Research Article

Catalytic Water Electrolysis by Co−Cu−W Mixed Metal Oxides: Insights from X-ray Absorption Spectroelectrochemistry

Nikita Gupta, Carlo Segre, Christean Nickel, Carsten Streb, Dandan Gao,* and Ksenija D. Glusac*

ACCESS | Metrics & More | Article Recommendations | Supporting Information

ABSTRACT: Mixed metal oxides (MMOs) are a promising class of electrocatalysts for the oxygen evolution reaction (OER) and hydrogen evolution reaction (HER). Despite their importance for sustainable energy schemes, our understanding of relevant reaction pathways, catalytically active sites, and synergistic effects is rather limited. Here, we applied synchrotron-based X-ray absorption spectroscopy (XAS) to explore the evolution of the amorphous Co−Cu−W MMO electrocatalyst, shown previously to be an efficient bifunctional OER and HER catalyst for water splitting. Ex situ XAS measurements provided structural environments and the oxidation state of the metals involved, revealing Co^{2+} (octahedral), $Cu^{+/2+}$ (tetrahedral/square-planar), and W^{6+} (octahedral) centers. *Operando* XAS investigations, including X-ray absorption near-edge structure (XANES) and extended X-ray absorption fine structure (EXAFS), elucidated the dynamic structural transformations of Co, Cu, and W metal centers during the OER and HER. The experimental results indicate that Co^{3+} and Cu^0 are the active catalytic sites involved in the OER and HER, respectively, while Cu^{2+} and W^{6+} play crucial roles as structure stabilizers, suggesting strong synergistic interactions within the Co−Cu−W MMO system. These results, combined with the Tafel slope analysis, revealed that the bottleneck intermediate during the OER is Co^{3+} hydroperoxide, whose formation is accompanied by changes in the Cu−O bond lengths, pointing to a possible synergistic effect between Co and Cu ions. Our study reveals important structural effects taking place during MMO-driven OER/HER electrocatalysis and provides essential experimental insights into the complex catalytic mechanism of emerging noble-metal-free MMO electrocatalysts for full water splitting.

KEYWORDS: electrocatalysis, mixed metal oxide, active species, X-ray absorption spectroscopy, water splitting
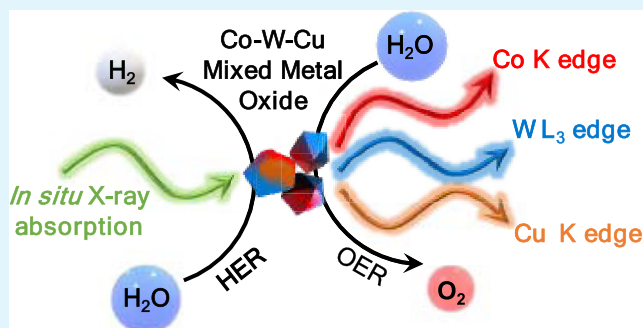
1. INTRODUCTION

Electrochemical splitting of water can be expressed in terms of the two half-reactions, namely, the oxygen evolution reaction (OER) and the hydrogen evolution reaction (HER), which can be used to generate green hydrogen a promising alternative to carbon-based fuels.[1,2] OER is considered the bottleneck of the water splitting, as it usually requires high overpotentials. The sluggish OER kinetics arise due to challenges associated with the formation of a weak O−O bond and the orchestration of four proton-coupled electron transfer steps at the desired potential. Traditionally, precious metal oxide (MO) catalysts, such as RuO_2 and IrO_2, have been used as benchmark OER catalysts with high catalytic activity. However, the high cost and scarcity in nature significantly limit their large-scale deployment.[3] As a result, researchers are exploring earth-abundant MOs based on transition metals such as Co, Mn, Ni, or Fe, as promising alternatives.[4−6] Remarkably, these non-noble MOs often perform better when combined into mixed metal oxides (MMOs), where synergetic effects boost the catalytic activity for both OER and HER.[7−10] For example, the Qiao group showed that the presence of Zn and Ni enhances

the HER activity of CoO, by providing an ideal environment for intermediate H-binding (by Ni^{2+}) and by boosting the electrical conduction (by Zn^{2+}).[9] In another example, the Nocera group has shown that the incorporation of Fe^{3+} into the NiO matrix increases the ability of the catalyst to access Ni^{4+} state, thus enhancing the OER performance.[11] Furthermore, the employment of MMOs as bifunctional catalysts also has the potential to simplify catalyst design and fabrication, reduce cross-contamination, and prevent catalyst poisoning, making them an attractive option for the production of green hydrogen.
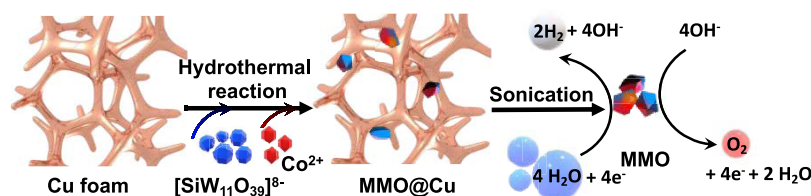
A comprehensive understanding of the catalytic mechanism of MMOs for the OER and HER is being actively explored. Based on computational studies, the OER in an alkaline

Scheme 1. Hydrothermal Synthesis of MMO for Water Electrolysis

medium is generally considered to occur via one of the two mechanistic pathways.[12,13] Pathway I, known as the adsorbate evolution mechanism, involves a single active site in which the activity is strongly correlated with the adsorption energies of the M−O intermediates. This pathway includes the formation of adsorbed M−OH species on the catalyst surface, their subsequent transformation to M−OOH, and the eventual release of O_2.[14,15] While pathway II, known as the lattice oxygen evolution mechanism, involves the participation of lattice oxygen in the oxide catalyst during O−O coupling and OER.[16,17] This pathway includes the direct combination of two M−O species, leading to the formation of the O_2 and the generation of active species. Similarly, the HER can occur via one of two reaction pathways, both of which involve electrochemical hydrogen adsorption as the first step in the catalytic reaction. In this context, pathway I proceeds via an electrochemical desorption step, which is known as the Volmer−Heyrovsky mechanism, while pathway II, known as the Volmer−Tafel mechanism, proceeds via H−H bond formation and chemical desorption route.[17,18] These mechanisms are analogous to the adsorbate evolution mechanism and the lattice oxygen evolution mechanism in the case of the OER, respectively.

However, the precise identification of catalytically active sites of MMO electrocatalysts is also attracting substantial attention. In this regard, ex situ characterization techniques can provide information regarding the atomic and electronic structures of the electrocatalyst pre- and postcatalytic OER/HER, while the *operando* investigation can shed light on the dynamic evolution of focused active sites over the catalytic process.[19,20] To this end, several different *in situ/operando* characterization techniques have been used to study OER processes, such as surface interrogation-scanning electrochemical microscopy (SI-SECM),[21] transmission electron microscopy (TEM),[22] Raman spectroscopy,[13] Fourier transform infrared spectroscopy (FTIR),[23] X-ray diffraction (XRD),[24] ambient pressure X-ray photoelectron spectroscopy (APXPS),[25] Fe Mössbauer spectroscopy,[26] resonant inelastic X-ray scattering (RIXS),[27] and electrochemical quartz crystal balance (EQCM).[28] In comparison to these techniques, X-ray absorption spectroscopy coupled with electrochemistry (XAS-EC) offers unique advantages in probing the chemical, electronic, and structural information on electrocatalysts. With XAS-EC, oxidation states, coordination environments, bond strengths, and catalytic intermediates of absorbed atoms on active species can be studied to gain real-time insight into molecule-based catalytic mechanisms under operating conditions.[13,29] In one instructive example, studies by the Abruña group identified the active sites as $Co^{2+/3+}$ and $Mn^{2+/3+/4+}$ redox couples for a bimetallic $Co_{1.5}Mn_{1.5}O_4/C$ catalyst system for OER and commented on the synergistic effect of Mn and Co.[30] In another example, the Boettcher group revealed the partial Fe oxidation and a shortened Fe−O bond length during

OER on the synthesized $Co(Fe)O_xH_y$ electrocatalyst, while only Co oxidation was observed in the absence of Fe cation, indicative of the essential role of Fe cation for OER.[31]

In this study, we delve into the structural dynamics of a versatile bifunctional electrocatalyst developed by the Streb group,[32] specifically the Co−Cu−W mixed metal oxide (MMO) electrocatalyst deposited on Cu foam by a general hydrothermal reaction involving Co ions and polyoxometalates (POM, $[SiW_{11}O_{39}]^{8-}$) precursors (Scheme 1, Co-ion: POM = 1:1). As compared to the recently reported POM-derived water splitting electrocatalysts (see Supporting Information (SI), Table S1), the obtained MMO on Cu foam is a competitive bifunctional electrocatalyst for OER and HER, with high stability over prolonged time (>10 h). Furthermore, the electrocatalysis was highly efficient: for the OER, the overpotential (at $j = 10$ mA/cm^2) was 313 mV and the Faradaic efficiency was ∼100%; for the HER, the overpotential (at $j = 10$ mA/cm^2) was 103 mV and the Faradaic efficiency was ∼98%. However, to date, the underlying electrochemical OER and HER mechanisms that enable the promising performance by the Co−Cu−W MMO remain unexplored.

Here, employing cutting-edge X-ray absorption spectroelectrochemistry (XAS-EC) at the Co and Cu K edges, as well as the W L_3 edge, we uncover the intriguing structural transformations of the MMO that occurs during water splitting. Through X-ray absorption near-edge structure (XANES), we gain precise knowledge regarding the oxidation states of the constituent metals, while extended X-ray absorption fine structure (EXAFS) unveils the structural changes of each metal center over electrocatalysis. In combination with Tafel slope analysis to derive information regarding the rate-determining step, these data allow us to propose plausible mechanisms for the catalysis of the OER and HER by the MMO. The OER was found to predominantly occur at the Co center, generating Co^{3+}-OOH as a bottleneck intermediate that undergoes a rate-determining release of molecular oxygen. Importantly, we have also identified interesting structural changes that take place at the neighboring Cu centers. While Cu does not undergo a change in the oxidation state, we discovered a lengthening of Cu−O bonds at Cu centers adjacent to Co^{3+}−OOH intermediates, which again points to a possible synergistic role of the Cu atoms to stabilize the Co^{3+}−OOH intermediates. Our Cu K edge XAS-EC results under cathodic conditions provide strong evidence for the formation of metallic Cu nanoparticles (Cu-NPs) whose size increases with the electrolysis time and the maximum diameter of ∼9 Å is achieved. We also observe changes in the Co−Cu distances and the change in the Co K edge energy, both of which are discussed in terms of the HER mechanism involving Cu-NPs and the rate-determining cooperative water dissociation step.
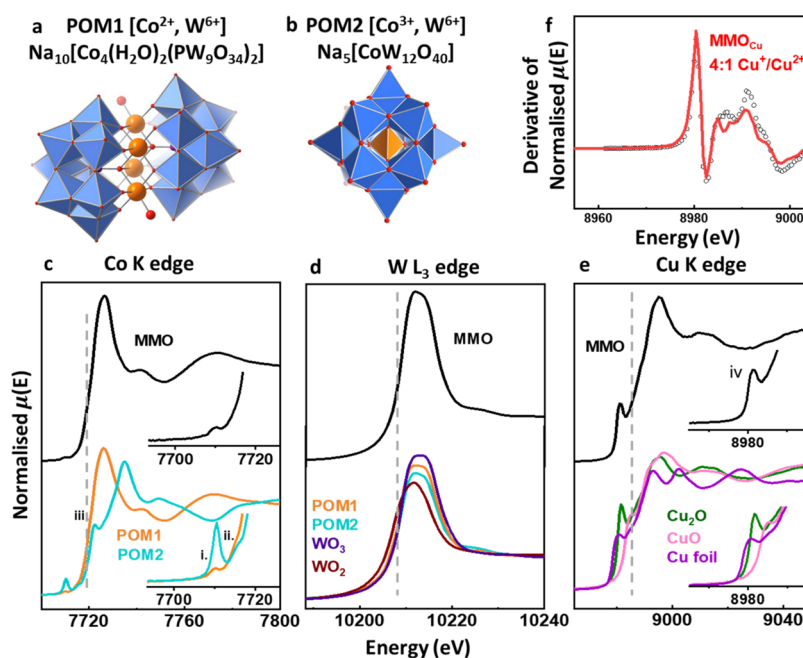
B

Figure 1. (a, b) Structures of POM1 and POM2; color scheme: Co atoms are in orange, O in red, and W in blue. Ex situ XANES spectra of (c) Co K edge, (d) W L$_3$ edge, and (e) Cu K edge of MMO and references, where the vertical dash line represents the edge energy. (f) Linear combination analysis of the MMO at Cu K edge.

2. EXPERIMENTAL SECTION

2.1. General. Chemicals and solvents were purchased from commercial sources (as indicated) and used without further purification. Na$_2$WO$_4$·2H$_2$O (223336, Sigma-Aldrich), tungsten(VI) oxide (214211000, ACROS Organics), copper(II) oxide (221281000, ACROS Organics), cobalt(II) oxide (44354, Alfa Aesar), tungsten-(IV) oxide (40367, Alfa Aesar), cobalt(II, III) oxide (AA4018414, Fischer Scientific), copper(I) oxide (566284, Sigma-Aldrich), CP: carbon paper (Toray Carbon paper, PTFE treated, TGP-H-60), nafion solution (42118, Alfa Aesar), and potassium hydroxide (221473, Sigma-Aldrich). IR measurements were performed on a Thermo Scientific Nicolet iS5 FTIR spectrometer to characterize the POMs. Inductively coupled plasma optical emission spectroscopy (ICP-OES) was performed on Agilent 5800 VDV ICP-OES (optical emission spectrometer) with the automatic sampler SPS 4. The samples were 10 times diluted with 5% nitric acid.

2.2. Fabrication of the MMO. The MMO (Co−W−Cu oxides) sample was prepared using a previously reported hydrothermal deposition route.[32] In brief, cleaned Cu foam (2 × 10 × 40 mm^3) was immersed in a Teflon autoclave liner containing an aqueous solution of Co(NO$_3$)$_2$·6H$_2$O (1.04 mmol) and K$_8$[SiW$_{11}$O$_{39}$]·13H$_2$O (1.0 mmol). The mixture was heated in an autoclave under autogenous pressure at 150 °C for 8 h, leading to a composite electrode with nanostructured MMO deposited on the surface (catalyst loading: ca. 1.25 mg/cm^2). The deposited MMO were removed from the Cu foam substrate by using prolonged sonication (10 h) in ethanol (Scheme 1).

2.3. Electrochemical Measurements. *2.3.1. MMO@CP Working Electrode Preparation.* 4 mg of the MMO was dispersed in a mixture of 280 μL of ethanol and 20 μL of 5.0 wt % Nafion followed by sonication for ca. 90 min to form a homogeneous suspension. 100 μL of the above suspension was drop-cast onto cleaned CP (controlled catalyst-loaded area: 1 cm^2), giving a catalyst loading of ca. 1.3 mg/cm^2 (based on geometric surface area). After being dried, the MMO@CP was further modified with a thin film of Nafion by drop-casting 20 μL of 0.5 wt % Nafion solution (diluted in isopropanol). Fresh electrode was used for each electrochemical measurement.

2.3.2. Electrocatalytic Oxygen and Hydrogen Evolution. Measurements were performed on a CH Instruments (CHI 760E)

workstation in a three-electrode configuration (working electrode: MMO@CP, reference electrode: saturated calomel electrode (SCE), counter electrode: platinum mesh) in 30 mL of 0.1 M aqueous KOH electrolyte (pH 12.8). All potentials were converted to the RHE, according to the Nernst equation ($E_{RHE} = E_{Hg/Hg_2Cl_2} + E_{SCE}^0 + 0.059$ V × pH, where $E_{SCE}^0 = 0.242$ V). Before data collection, the working electrode was preconditioned by 20 cyclic voltammetry (CV) scans (at 100 mV/s) between 0.2 and 0.5 V vs the RHE to ensure stable electrochemical performance at room temperature. Polarization curves were recorded by linear sweep voltammetry (LSV) at a scan rate of 5 mV/s with 80% iR compensation.

2.4. XAS Measurements. XAS measurements at Co K edge, Cu K edge, W L$_3$ edge X-ray absorption near-edge structure (XANES) and extended X-ray absorption fine structure (EXAFS) experiments were carried out at beamline 5-BM-D of DND-CAT, Advanced Photon Source, Argonne National Laboratory. A Vortex ME4 detector was used to collect the fluorescence signal, while a Si (111) monochromator scanned the incident X-ray photon energy through the Cu/Co K and W L3 absorption edges. The X-ray beam was calibrated using respective metal foil. No sample damage was detected at the beamline, as consecutive scans did not show any changes over time.

2.4.1. Ex Situ XAS Measurements. Thin films of powder samples were deposited on top of Scotch tape to fulfill the transmission detection requirements with X-ray attenuation of 0.1−1 at the respective edge. Energy calibration was performed using the respective metal foil placed behind the sample. The data were collected in the transmission mode. The X-ray beam was calibrated by using metal foil. Data reduction, analysis, and EXAFS fitting were performed with the Athena, Artemis, and IFEFFIT software packages (see Section S2, SI). Fourier transform of EXAFS was performed using the Hanning window function with k-weights of 2. The pre-edge background was linearly fitted and subtracted. The post-edge background was determined using a cubic-spline-fit procedure and then subtracted. Normalization was performed by dividing the data by the height of the absorption edge at 50 eV.

2.4.2. EXAFS Fitting. The data were normalized and background subtracted to obtain the $\chi(k)$ and then weighted by k^2. Fourier transform was taken on the data from the shown k window, and the fits were performed in R space over the range of the shown window

using metal−oxygen and metal−metal scatterings. All metal foil (Cu, Co, and W) data were fitted to their respective crystal structure to obtain amplitude reduction factor (S_0^2) values. With S_0^2 known, the EXAFS data of the catalyst materials were fitted with such generated phase shifts and amplitudes (see Section S3, SI). For the Co K edge of POM1 and POM2 samples (see section 3), POM model-based EXAFS analysis was done using scattering paths generated by the FEFF calculation function in Artemis based on their respective crystal structure. For the W L_3 edge of POM1 and POM2 samples, scattering paths were generated by taking weighted average bond lengths of different W−O and W−Co scattering paths from the crystal structure. Nine and three different W environments were seen in POM1 and POM2, respectively.

2.4.3. XAS-EC Studies in the Lab-Made Cell. The MMO@CP was mounted onto a custom-designed XAS-EC three-electrode 10 mL XAS fluorescence cell (Figure S9). A Pt wire (MW-4130 or MW-1033, Basi research) and a saturated calomel electrode (EF-1352, Basi research) were used as the counter and reference electrodes in Ar purged 0.1 M aqueous KOH electrolyte, respectively. Cu/Co K and W L_3 absorption edges were collected under various applied potentials controlled by a Gamry 1010B electrochemical workstation. Each selected potential (80% iR compensation) was held until enough data statistics from XAS were achieved. The X-ray beam was calibrated using the respective metal foil. The one-compartment electrolysis cell contained an X-ray transparent window, where the solution-facing side of MMO@CP served as the working electrode (Figure S10). This configuration prevented interference from the electrolyte solution or catalytic bubbles. Potentials of +1.68 and −0.4 V *vs* RHE were applied for the OER and HER, respectively, and the corresponding XAS spectra were collected throughout the potential controlled measurement. A thin film of catalyst ink was drop-cast on CP to observe the reactive species to ensure that XAS spectra were representative of electrolyte-exposed MMO. Because of the small amount of MMO on the CP, a total of 12 scans were averaged to yield the spectrum. Sustained currents indicative of the HER or OER were observed throughout data collection. By analyzing the Co K edge, Cu K edge, and W L_3 edge XAS spectra, we aimed to elucidate the changes in the oxidation states and coordination environments of the catalyst active sites. Fresh electrodes were used for every electrochemical measurement.

3. RESULTS AND DISCUSSION

3.1. Ex Situ XAS. Ex situ XANES and EXAFS were performed to comprehensively investigate the oxidation states and coordination environments of Co, W, and Cu elements in the MMO. To this end, two model polyoxometalates (POM) were synthesized as references: POM1 ($Na_{10}[Co_4(H_2O)_2(PW_9O_{34})_2]$, Figure 1a) containing Co^{2+} and W^{6+} and POM2 ($Na_5[CoW_{12}O_{40}]$, Figure 1b) containing Co^{3+} and W^{6+}.[33−35] Synthetic routes and characterization details are listed in SI. As shown in Figure 1c, the ex situ Co K edge XANES spectra of POM1 demonstrate weak pre-edge features at 7710.6 eV and an edge energy of 7719 eV. Additionally, the pronounced white line characteristic implies an octahedral (O_h) coordination environment for the Co ions in POM1.[31] In contrast, POM2 exhibits distinct spectral features with a strong pre-edge peak (i: 7710.5 eV, assigned to the 1s → t_{2g} transition) and a weak peak (ii: 7716.0 eV, assigned to the 1s → e_g transition), indicative of a noncentrosymmetric tetrahedral (T_d) arrangement of the Co ions in POM2.[31] Furthermore, POM2 displays a visible rising edge peak (iii: 7722.5 eV, 1s → 4p) with an edge energy of 7720.5 eV. These geometry assignments are consistent with the previously reported XANES of relevant Co-complexes (e.g., $Na_{10}[Co_4(H_2O)_2(VW_9O_{34})_2]·35H_2O$, $K_5[CoW_{12}O_{40}]·20H_2O$).[33−35]

The Co K edge spectrum of the MMO (Figures 1c and S1a, SI) is free of the strong pre-edge features existing in POM2, while it shows substantially matching edge energy (7719 eV) and white line peak energy to those of POM1, indicative of Co^{2+} oxidation state and O_h geometry of the Co ions in the MMO. According to Figure 1d (Figure S1b, SI), the ex situ XANES W L_3 edge spectra of the MMO show an edge energy of 10204.6 eV, which is nearly identical to that of W^{6+} containing references POM1, POM2, and WO_3 and significantly different from the W^{4+} reference WO_2. In addition, the broad white line feature shown in POM1, POM2, and WO_3[36,37] was also observed in MMO, demonstrating the O_h coordination geometry of the W in W^{6+} oxidation state. The ex situ XANES Cu K edge spectrum of MMO shows a sharp edge peak (1s → 4p) at 8981.4 eV (labeled as iv, inset Figures 1e and S1c, SI) and the absence of the pre-edge peak features existing in the Cu^{2+} reference (CuO, 8979 eV, 1s → 3d).[38] Additionally, the MMO shows an edge energy of 8985 eV, which is between that of Cu^+ (8984 eV) and Cu^{2+} (8986 eV),[39,40] suggesting the presence of a mixture of Cu^+ and Cu^{2+} in the MMO. This is further confirmed by the linear combination analysis, giving a ratio of 4:1 (Cu^+/Cu^{2+}, Figure 1f and Table S2, SI).[41]

The experimental ex situ EXAFS data obtained for POM1 and POM2 at the Co K and W L_3 edges were fitted with good-to-excellent results using scattering paths based on their structures obtained previously via single-crystal X-ray diffraction (R- and K-space fitting of POM1 and POM2 data are shown in Figures S2−S3 and Table S3, SI).[33−35] As shown in Figure 2, the dominant interaction in both POM1 and POM2
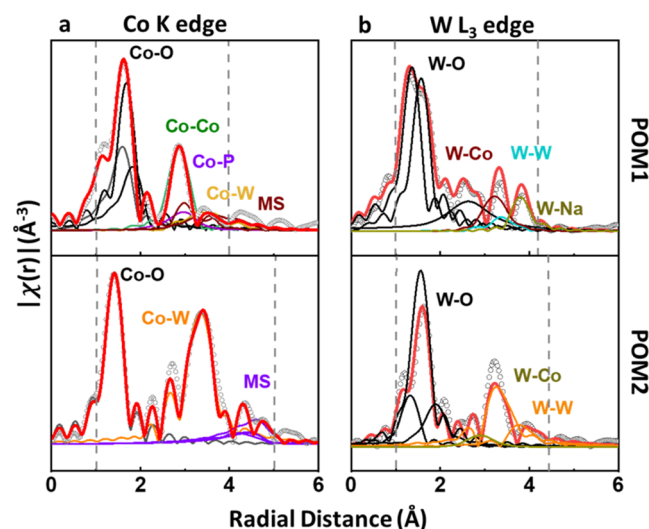

Figure 2. Ex situ EXAFS of POM references. (a) Co K edge of POM1 (top) and POM2 (bottom), (b) W L_3 edge of POM1 (top) and POM2 (bottom), where the experimental data is in circles and fitted data is the red solid line. Individual path lengths are shown with solid lines. MS: multiple atom scattering paths.

are the metal−oxygen scattering paths with average bond lengths of 2.019 ($n = 2$), 2.086 ($n = 2$), and 2.258 Å ($n = 2$) in POM1 and 1.805 Å ($n = 4$) in POM2 (n: the number of scattering paths). This highlights the critical role of the metal−oxygen coordination environment in shaping the overall structural characteristics of both model POMs. Furthermore, an in-depth analysis of the second shell fitting of POM1 revealed intense Co−Co scattering at 3.2 Å and weak Co−W
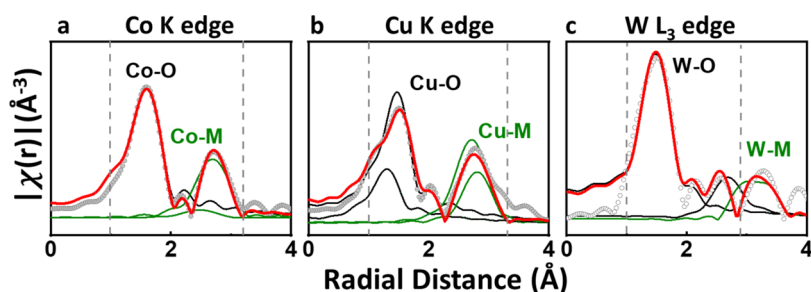
Figure 3. EXAFS data fitting of (a) Co K edge, (b) Cu K edge, and (c) W L$_3$ edge of MMO where the experimental data are in circles and fitted data are the red solid line. Solid gray dash lines show the data window that has been fitted. Metal−oxygen scattering is shown in black, and metal−metal scattering is shown in green.

scattering at 3.5 Å, indicating the presence of neighboring Co and W atoms. In contrast, a pronounced Co−W scattering at ca. 3.5 Å was observed in POM2, consistent with the exclusive Co−W environment.

Following the structural studies of model POMs, we investigated the ex situ Co K edge, Cu K edge, and W L$_3$ edge EXAFS spectra of the MMO (Figure 3 and Table 1). The

Table 1. Summary of Structure Information of MMO

	Co K edge	Cu K edge	W L$_3$ edge
oxidation state	Co^{2+}	Cu^{+}/Cu^{2+}	W^{6+}
geometry	O$_h$	T$_d$/SP	O$_h$
fitted bond lengths (X = Cu, Co)	Co−O: 2.07 Å	Cu−O: 1.85 Å, 1.96 Å	W−O: 1.88 Å, 3.01 Å
	Co−X: 2.89 Å, 3.06 Å	Cu−X: 3.00 Å, 3.13 Å	W−X: 3.37 Å

first shell of the Co K edge EXAFS data for MMO was successfully fitted using an O$_h$ CoO$_6$ geometry with a Co−O bond length of 2.07 Å. In addition, the second coordination shell revealed two distinct scattering paths, Co−X at distances

of 2.89 Å (n = 2) and 3.06 Å (n = 6). The identity of X can either be Co or Cu, as both metals have similar atomic numbers and therefore gave equally good fits to the experimental data (Figure S4 and Table S4, SI).[42] Notably, no Co−W scattering was observed in the Co K edge EXAFS, which is either due to a small number of neighboring W atoms (similar to the EXAFS of POM1, Figure 2a), or a completely W-free environment.[35]

The Cu K edge EXAFS data were fitted using a combination of two types of Cu environments, in agreement with the presence of Cu^{2+} (20%) and Cu^{+} (80%) ions revealed in the XANES Cu K edge results. The first shell of Cu^{+} species was modeled as T$_d$ CuO, while the Cu^{2+} species was modeled as square-planar (SP) Cu$_2$O, and the Cu−O bond lengths obtained from the fit were 1.85 Å (n = 3) and 1.96 Å (n = 1), respectively, which is in line with literature reports on comparable samples.[43,44] Additionally, the secondary coordination sphere fitting revealed two distinctive Cu−X peaks with bond lengths of 3.00 Å (n = 6) and 3.12 Å (n = 3) (here, X = Co or Cu, Figure S5 and Table S5, SI).

The EXAFS analysis at the W L$_3$ edge was performed using an O$_h$ WO$_6$ first shell with two bond lengths at 1.88 Å (n = 3)
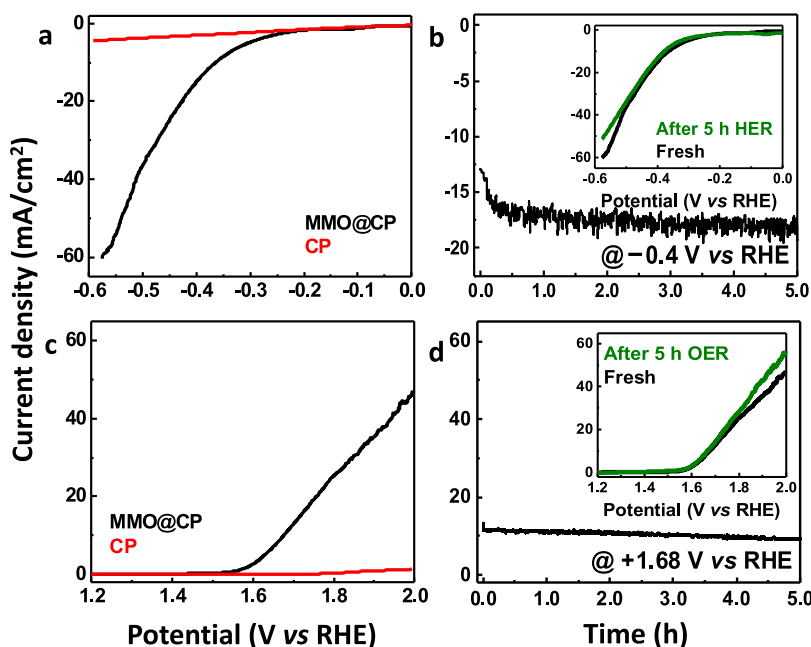

Figure 4. Catalytic performance of MMO@CP for the HER and the OER. LSV polarization curves of MMO@CP and CP reference for HER (a) and OER (c), scan rate: 5 mV/s; chronoamperometric studies of (c) HER (−0.4 V vs RHE) and (d) OER (+1.68 V vs RHE); inset: LSV comparison of HER and OER performance.
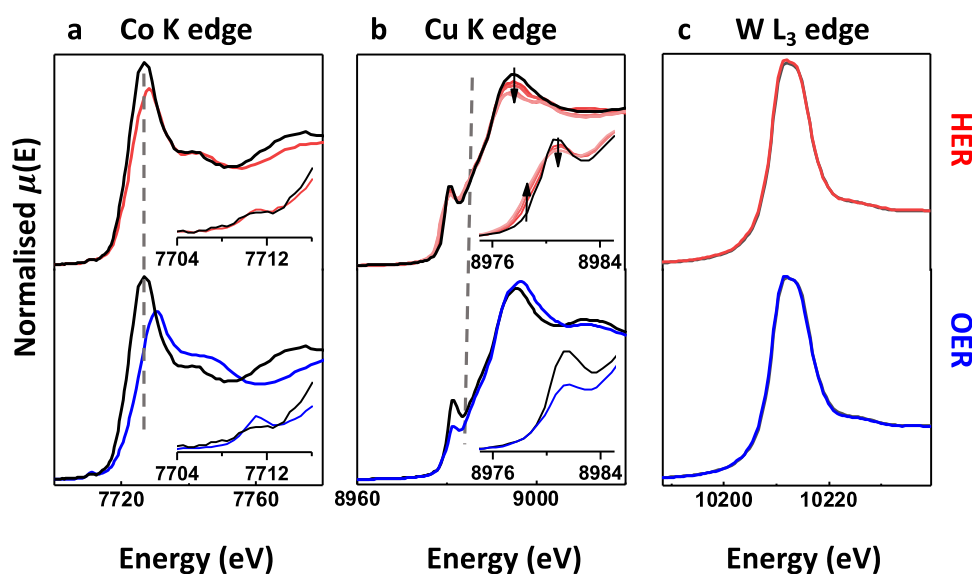
E

Figure 5. XAS-EC XANES spectra of (a) Co K edge, (b) Cu K edge, and (c) W L3 edge of MMO under −0.4 V *vs* RHE (for HER), +0.65 V *vs* RHE (for OCP) and +1.68 V *vs* RHE (for OER). The insets show the pre-edge region of the corresponding curves.

and 3.01 Å ($n = 3$, Figure 3c). This observation implies the existence of either two distinct WO_6 O_h environments in a 1:1 ratio or one distorted trigonal prismatic configuration. The trigonal prismatic configuration of WO_6 is rare, but it has been observed in mixed metal oxides with AABB packing arrangement of metal-oxo clusters.[45] Moreover, the presence of a second metal site (possibly Co or Cu) was detected at a distance of 3.37 Å ($n = 2$). Notably, no W−W scattering paths were observed, suggesting that all W atoms in the MMO are isolated and surrounded by Co or Cu metal oxides (Figure S6 and Table S6, SI). These extensive ex situ characterizations lay a solid foundation for subsequent *operando* XAS studies, which will contribute to an in-depth understanding of the dynamic structural evolution of the MMO as well as the potential catalytic mechanism.

3.2. XAS-EC. Prior to the XAS-EC studies, the electrocatalytic performance of the solid-state MMO (drop-cast on carbon paper, MMO@CP) was examined for both HER and OER in an alkaline aqueous electrolyte (0.1 M aqueous KOH, pH 12.8). Linear sweep voltammetry (LSV) polarization curves (Figure 4a,c) show that the MMO@CP exhibits suitable electrocatalytic activity, with overpotentials of 365 and 447 mV for HER and OER at a current density j of 10 mA/cm^2 (based on geometric surface area). The overpotential is somewhat higher than the previously reported composite electrode (MMO@Cu),[32] which we attribute to the different electrode support (CP instead of Cu foam), resulting in a less ideal electrode/catalyst interaction. However, for the targeted XAS study, the increased overpotentials do not pose a problem. Importantly, MMO also outperforms the bimetallic reference sample (Ref. 1, Co−Cu oxide, obtained by the absence of POMK$_8$[SiW$_{11}$O$_{39}$]·13H$_2$O) in the precursor solution) as well as a wide range of commercial single metal oxides (for details, see Figure S7, SI). Notably, we also observed that on deploying different precursor compositions by varied Co-ion/POM ratios of 1:2 and 2:1 on Cu foam leads to less active composite electrodes with different surface metal oxides composition (for details, see Figure S8, SI). These results indicate the underlying synergistic effect among the metals involved in the MMO for both OER and HER.

Next, to assess the long-term stability of the MMO@CP, chronoamperometry was conducted over 5 h. The current density was stable under both HER and OER conditions, and the comparison of LSV curves before and after 5 h of electrolysis (insets in Figure 4b,d) displayed nearly identical performance, with relatively no leaching of any of the metals in the solution (Table S7). The current density for the HER exhibited an initial increase, hinting at the possible electrochemical generation of the catalytically active species (Figure 4b). Note that the role of the counter electrode on the observed HER activity was eliminated by comparing the results with those obtained using graphite as the counter electrode (Figure S9, SI).[46] For OER, the activity remained at 82% activity after the 5 h period (Figure 4d), demonstrating the stability of the MMO@CP model electrode under harsh oxidative electrocatalytic conditions.[26]

To gain critical insights into the structural evolution of the MMO under operating conditions, the XAS-EC measurements were conducted at open-circuit potential (OCP) and electrocatalytic potentials (+1.68 V vs RHE for the OER and −0.4 V vs RHE for the HER) using a custom-built spectro-electrochemical cell (Figure S10, SI). The Co K edge XANES spectra observed under the OER conditions (Figure 5a) show a noticeable positive shift of the edge energy (from 7719 to 7722 eV), indicative of the oxidation of Co^{2+} to Co^{3+}. This transformation is further supported by the oxidation state analysis involving the integration of the XANES area under the edge from $\mu(E) = 0.1$ to 1 (Figure S10, SI).[47] Additionally, the increase in the intensity of the pre-edge peak (7711 eV, s → d, Figure 5a, inset) is expected for the loss of a 3d electron during Co^{2+} to Co^{3+} oxidation. The increased pre-edge intensity is also considered as a reporter of a deviation from the centrosymmetric O_h geometry. This reduction in symmetry is known to lead to increased 3d−4p hybridization of the metal orbitals, thus increasing the "allowedness" of the 1s → 3d transition.[48,49] In contrast, under HER conditions, no edge energy changes were observed (Figure S11, SI), indicating that the original Co^{2+} oxidation state is retained. The increased pre-edge peak intensity and the expansion of the white line region demonstrate a change in the coordination environment around
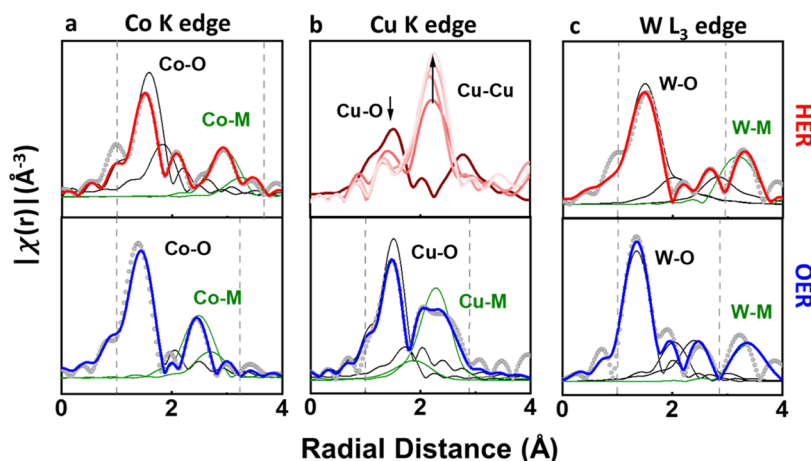
Figure 6. XAS-EC EXAFS measurement of (a) Co K edge, (b) Cu K edge, and (c) W L3 edge of MMO@CP under −0.4 V *vs* RHE (for HER in red), 0 V *vs* RHE (for OCP in brown), and +1.68 V *vs* RHE (for OER in blue). Gray line: M−O scattering, green line: M−M scattering, vertical dash line: r region of *R* space used for fitting, gray circles: experimental data.

the Co site during both OER and HER, suggesting that Co sites play an active role during both catalytic processes.

The Cu K edge XANES spectra (Figure 5b) exhibit no significant changes in pre-edge and edge energies (from 8985 to 8984.9 eV) during the OER, implying that no oxidation state changes occur at the Cu centers during the OER. In contrast, a shift of the Cu edge energy to lower values (from 8985 to 8984.5 eV, Figure S12, SI) was observed during the HER, implying the reduction of Cu^+/Cu^{2+} ions to metallic Cu species. Linear combination analysis of these scans also indicated the formation of metallic Cu (from 0 to 62.9%), while Cu^+ was found to be diminished (from 80 to 21.6%) and Cu^{2+} slightly decreased (from 20 to 15.5%) (Table S8 and Figure S13, SI). This dynamic transformation suggests that the Cu^+ sites are the precatalytic species that are electrochemically reduced to the catalytically active Cu-NPs.

The W L$_3$ edge XANES spectra displayed no discernible changes in either the OER or HER (Figure 5c). The stability of the W sites implies that these sites might act as a redox-inactive spectator, which provides structural support to the OER/HER active Co and Cu sites. Furthermore, the absence of significant changes in the W coordination environment observed by the retained broad white line features indicates that the W atoms remained isolated and surrounded by Co or Cu metal oxide species. For a summary of the structural changes of Co, Cu, and W in the MMO, see Table S9, SI.

Next, XAS-EC EXAFS measurements were performed to capture the local structural evolution of the MMO during electrocatalytic water splitting. Analysis of the Co K edge EXAFS during OER implies the retention of the O$_h$ geometry and the shortening of the Co−O bond length from 2.07 to 1.9 Å, expected for Co hydroperoxide species intermediate,[50] along with a decrease in distance for one of the Co−X pathways (from 3.06 to 2.9 Å, Figure 6a). Under HER conditions, the O$_h$ coordination environment of Co undergoes a distortion characterized by a pronounced elongation of Co−O bonds (from 2.07 to 2.27 Å), while the length of the other four Co−O bonds remains unchanged. Simultaneously, there was an increase in the Co−X bond length from 2.89 to 3.56 Å ($n = 2$) and 3.06 Å ($n = 6$) to 3.25 Å ($n = 4$) (Table S10 and Figure S13, SI). Detailed analysis of changes in these bond lengths has been discussed in more detail in the following Section 3.3.

The analysis of the Cu K edge EXAFS spectra during the OER shows that both Cu moieties remain in the original coordination environment, with Cu−O bond lengths increasing from 1.85 to 1.93 Å ($n = 3$, Cu^+), and from 1.96 to 2.16 Å ($n = 1$, Cu^{2+}, Figure 6b). Furthermore, the bond length for Cu−X decreases from 3.0 Å ($n = 6$) to 2.59 Å ($n = 6$), and from 3.12 Å ($n = 3$) to 2.26 Å ($n = 2$), see Figure S15 and Table S11, SI.[51] More drastic EXAFS changes were observed during HER, where Cu species underwent a compositional transformation to metallic Cu-NPs, observed as the growth of the new Cu−Cu scattering feature at 2.7 Å (Figures 6b and S16 and Table S12, SI). This feature grows with electrolysis time from $n = 0$ to 7 over the period of 4 scans. We assign this to the *operando* formation of metallic Cu-NPs under reducing electrochemical conditions. The size of these Cu-NPs was evaluated based on the number of Cu−Cu scattering paths, using the calibration curve obtained for Cu−Cu scattering in NPs with known diameters, reported in the previous studies.[52−54] We find that the Cu-NP diameter increases over the time of XAS-EC scans, reaching approximately 9 Å (a cluster of ∼97 Cu atoms; for calculation details, see the SI) by the end of our experiments.

Based on the W L$_3$ edge EXAFS spectra (Figure 6c), the O$_h$ coordination environment around W became more distorted during both the OER and HER. OER was accompanied by the decrease in one W−O bond length from 3.01 Å ($n = 3$) to 2.46 Å ($n = 1$) and 2.83 Å ($n = 2$), while the other remained constant within the error limit (1.88 Å, $n = 3$). In contrast, the length of one W−O bond was reduced from 3.01 Å ($n = 3$) to 2.35 Å ($n = 1$) under HER conditions, while the other W−O bond lengths (1.88 Å ($n = 3$) and 3.01 Å ($n = 2$)) remained unchanged (Figure S17 and Table S13, SI). No significant changes in W−X bond lengths were observed.[51]

3.3. Mechanisms. Insights into HER and the OER mechanisms were obtained by combining electrochemical Tafel slope analysis and XAS-EC data fitting. For HER, Tafel slopes exceeding 120 mV/decade (theoretical limit for Tafel slope analysis for HER) were obtained for the MMO@CP (142−208 mV/decade, Figure S18a, SI), while even higher Tafel slopes were observed in the previous study on the composite MMO@Cu electrode (335 mV/decade).[32] Notably, such high Tafel slopes have been reported for HER in basic media, where the water dissociation step ($H_2O \rightarrow H^+ + OH^-$)

was proposed as the rate-determining step (RDS).[55−57] In this context, it should be the formation of the M−H bond. According to the XAS-EC data, the Co and Cu centers demonstrated chemical and structural evolution during HER (Figures 5 and 6). Notably, only the Cu+ center underwent a change in the oxidation state from Cu+ to Cu0, which gave rise to the formation of Cu-NP (new Cu−Cu peak at 2.7 Å), while the Co centers maintained their original Co2+ states, along with the elongation of both Co−X and Cu−X around 3.2 Å, indicating the presence of neighboring Co and Cu atoms under reductive conditions. Based on these findings, we propose a mechanism that involves the electrochemical conversion of MMO (Cu+-oxo/Co2+-aqua), to catalytically active Cu-NP/Co2+−OH site,[58] where Cu−Co scattering distance increases due to the structural rearrangement that accompanies the nanoparticle formation. We hypothesize that the presence of neighboring Co centers helps in the water dissociation steps by acting as a proton source to form surface Cu−H/Co2+−(OH)2 species during the RDS (Figure 7), resulting in increased Co−
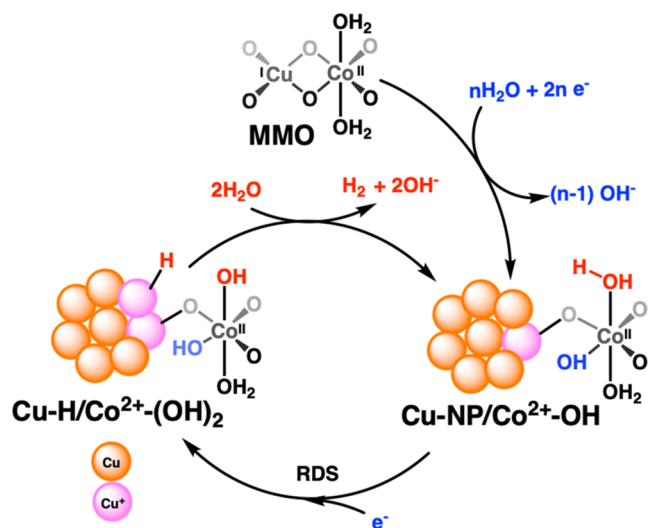

Figure 7. Proposed mechanism for HER by *operando* formed Cu-NPs on the MMO electrocatalyst.

Cu, Co−O, and decreased Cu−Cu scattering path lengths. The subsequent H2 releasing step may occur via either the Heyrovsky or Tafel pathways. The established reactivity of Cu-NPs in the literature further supports this observation.[59−61] It is likely that the nanostructured Cu sites (Cu-NP/Co2+−OH)

exhibit improved HER kinetics by exposing more active sites on the Cu surface.[62]

For OER, the Tafel slopes were derived for two possible OER mechanisms: single-site (SS) and double-site (DS) models.[63] Both mechanisms involve the formation of M−OH and M=O intermediates on the MMO surface, where M denotes an active site on the surface of the MMO catalyst

$$M + OH^- \rightarrow M{-}OH + e^- \tag{1}$$

$$M{-}OH + OH^- \rightarrow M = O + H_2O + e^- \tag{2}$$
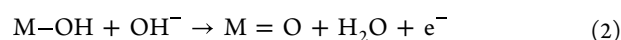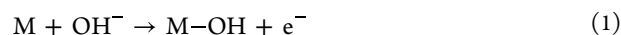
The SS model proceeds via the formation of the MOOH intermediate

$$M = O + OH^- \rightarrow MOOH + e^- \tag{3}$$

$$MOOH + OH^- \rightarrow M + O_2 + e^- \tag{4}$$
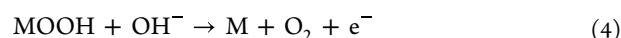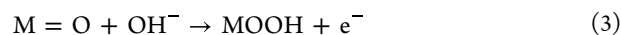
While the DS model proceeds via the bimetallic O−O coupling

$$2M = O \rightarrow M + O_2 \tag{5}$$
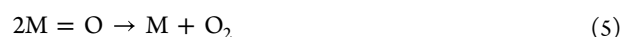
The derivation of Tafel slopes assuming different rate-determining steps is shown in the SI (Section S5.1, SI), while the simulated Tafel slopes are shown in Figure 8a. Different RDSs can be distinguished at low overpotentials, where a 120 mV/decade slope is expected when Step 1 is the RDS. The Tafel slopes of 40, 23.6, 16, or 14 mV/decade are expected when Step 2, Step 3, Step 4, or Step 5 is the RDS. Experimental Tafel slopes of the MMO were derived from LSV data (Figures 8b and S18b, SI), illustrating values increasing from 16 mV/decade at 0.07 V overpotential to 180 mV/decade at 0.25 V overpotential. Given that the experimental slope drops below 20 mV/decade at low overpotentials (0.07 V), we hypothesize that the RDS is the release of O2, either via Step 4 (for the SS mechanism with a Tafel slope of 16 mV/decade) or via Step 5 (for the DS mechanism with a Tafel slope of 14 mV/decade). In this context, the intermediates for the OER bottleneck are identified to be the formation of either MOOH (for the SS mechanism) or M=O (for the DS mechanism).

According to the XAS-EC data, the Co and Cu centers demonstrated chemical and structural evolution during the OER (Figures 5 and 6). Notably, only the Co center underwent a change in the oxidation state from Co2+ to Co3+, while the Cu centers maintained their original Cu+/2+ states. Based on these observations, SS mechanism was proposed involving Co3+−OOH (observed during XAS-EC) as the bottleneck intermediate before the RDS of the O2
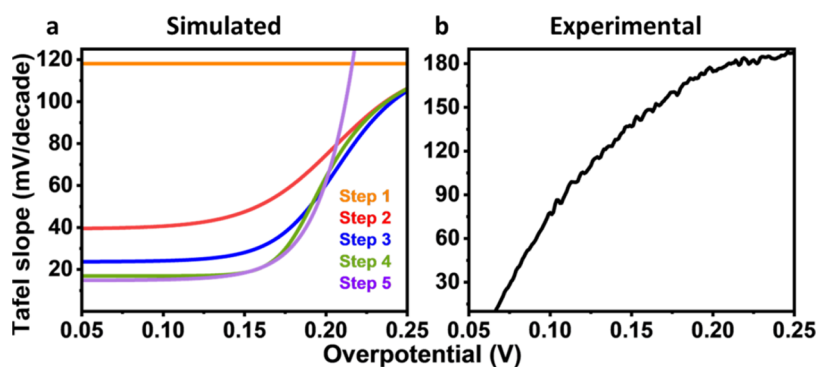

Figure 8. (a) Simulated and (b) experimental Tafel slope analyses for the OER.

evolution. As depicted in Figure 9, the catalytic cycle includes cooperative catalysis by a redox-active Co center, $Co^{2+}-H_2O$
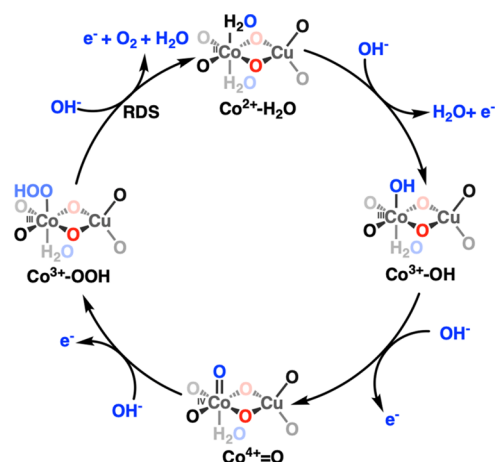

Figure 9. Proposed mechanism of the SS model for the OER.

(MMO), and redox-innocent Cu. This proposed mechanism is supported by the XAS-EC data, which show the elongation of Cu−O and the compression of Co−O bond lengths in intermediate $Co^{3+}-OOH$, a structural change that is consistent with the increased charge of the Co^{3+} center. This change in the Co−O−Cu bond lengths indicates the mechanism by which the neighboring Cu atoms tune the reactivity of the $Co^{3+}-OOH$ intermediate, facilitating the evolution of O_2. Previous studies involving mixed metal Co−Cu oxides and sulfides have also reported a synergy between the two metals during OER.[64−66] In general, the synergy was attributed to the modulation of reactive, high-spin, O_h Co^{3+} intermediates, and these conclusions are in good agreement with our experimental observations. Specifically, the observation of bond length changes in the Co−O−Cu moiety may be a structural change critical for the formation of either more reactive or more stabilized Co^{3+}-hydroperoxides and may be explored as a criterion for the design of future improved MMO catalysts.

4. CONCLUSIONS

In summary, by employing synchrotron-based XAS, combined with Tafel slope analysis, we reveal the complex catalytic behavior exhibited by the Co−Cu−W MMO@CP under alkaline HER and OER. The HER was found to proceed via *operando* formation of catalytically active $Cu-NP/Co^{2+}-OH$, electrogenerated from the Cu^+-oxo/Co^{2+}-aqua (MMO) precatalysts. Specifically, the presence of neighboring Co facilitates the water dissociation step by forming the Cu−H/$Co^{2+}-(OH)_2$ intermediate during the RDS. Furthermore, during the electrolysis process, the Cu-NPs formed *in situ* showed an interesting dynamic evolution as their diameter increased gradually over time. The OER was found to proceed via a $Co^{3+}-OOH$ bottleneck intermediate, whose electronic behavior and structure are tuned by the neighboring Cu atoms. The identification of key redox-active centers, determination of RDS, and revelation of intermediates, is a substantial leap in our understanding of the fundamental mechanisms of electrocatalytic water splitting driven by mixed metal oxide electrocatalysts. In future, this insight will guide the knowledge-based design of efficient MMO electrocatalysts, and also highlights the importance of synergistic interactions within

MMO systems, thereby laying a solid foundation for the design of next-generation electrocatalysts for challenging energy conversion and storage reactions.

■ ASSOCIATED CONTENT

Ⓢ Supporting Information

The Supporting Information is available free of charge at https://pubs.acs.org/doi/10.1021/acsami.4c06365.

> Materials synthesis and characterization; experimental details for XAS measurements, and Tafel slope derivation for different OER steps (PDF)

■ AUTHOR INFORMATION

Corresponding Authors

Dandan Gao − Department of Chemistry, Johannes Gutenberg University Mainz, Mainz 55128, Germany; Email: dandan.gao@uni-mainz.de

Ksenija D. Glusac − Department of Chemistry, University of Illinois Chicago, Chicago, Illinois 60607, United States; Chemical Sciences and Engineering, Argonne National Laboratory, Lemont, Illinois 60439, United States; ⓞ orcid.org/0000-0002-2734-057X; Email: glusac@uic.edu

Authors

Nikita Gupta − Department of Chemistry, University of Illinois Chicago, Chicago, Illinois 60607, United States; Chemical Sciences and Engineering, Argonne National Laboratory, Lemont, Illinois 60439, United States

Carlo Segre − Department of Physics & Center for Synchrotron Radiation Research and Instrumentation, Illinois Institute of Technology, Chicago, Illinois 60616, United States; ⓞ orcid.org/0000-0001-7664-1574

Christean Nickel − Department of Chemistry, Johannes Gutenberg University Mainz, Mainz 55128, Germany

Carsten Streb − Department of Chemistry, Johannes Gutenberg University Mainz, Mainz 55128, Germany; ⓞ orcid.org/0000-0002-5846-1905

Complete contact information is available at:
https://pubs.acs.org/10.1021/acsami.4c06365

Author Contributions

N.G., C.S., D.G., and K.D.G. conceived the research idea. N.G., D.G., and C.N. performed materials synthesis and electrocatalytic studies. Gupta and Segre carried out XAS-EC and data analyses. D.G., C.S., and K.D.G. acquired funding and provided project administration. The manuscript was written and reviewed through contributions of all authors. All authors have given approval to the final version.

Notes

The authors declare no competing financial interest.

■ ABBREVIATIONS

XAS, X-ray absorption spectroscopy; XANES, X-ray absorption near-edge structure; EXAFS, extended X-ray absorption fine structure; XAS-EC, X-ray absorption spectro-electrochemistry; RDS, rate-determining step; MMO, mixed metal oxide; Oh, octahedral; Td, tetrahedral; SP, square-planar; Cu-NP, copper nanoparticle

■ REFERENCES

(1) Ifkovits, Z. P.; Evans, J. M.; Meier, M. C.; Papadantonakis, K. M.; Lewis, N. S. Decoupled Electrochemical Water-Splitting Systems: A Review and Perspective. *Energy Environ. Sci.* **2021**, *14*, 4740−4759, DOI: 10.1039/d1ee01226f.

(2) Lamers, P.; Ghosh, T.; Upasani, S.; Sacchi, R.; Daioglou, V. Linking Life Cycle and Integrated Assessment Modeling to Evaluate Technologies in an Evolving System Context: A Power-to-Hydrogen Case Study for the United States. *Environ. Sci. Technol.* **2023**, *57* (6), 2464−2473.

(3) Geletii, Y. V.; Huang, Z.; Hou, Y.; Musaev, D. G.; Lian, T.; Hill, C. L. Homogeneous Light-Driven Water Oxidation Catalyzed by a Tetraruthenium Complex with All Inorganic Ligands. *J. Am. Chem. Soc.* **2009**, *131* (22), 7522−7523.

(4) Yu, M.; Budiyanto, E.; Tüysüz, H. Principles of Water Electrolysis and Recent Progress in Cobalt-, Nickel-, and Iron-Based Oxides for the Oxygen Evolution Reaction. *Angew. Chem., Int. Ed.* **2022**, *61*, No. e202103824, DOI: 10.1002/anie.202103824.

(5) Wang, M.; Wa, Q.; Bai, X.; He, Z.; Samarakoon, W. S.; Ma, Q.; Du, Y.; Chen, Y.; Zhou, H.; Liu, Y.; Wang, X.; Feng, Z. The Restructuring-Induced CoOxCatalyst for Electrochemical Water Splitting. *J. Am. Chem. Soc.* **2021**, *1* (12), 2216−2223.

(6) Huynh, M.; Bediako, D. K.; Nocera, D. G. A Functionally Stable Manganese Oxide Oxygen Evolution Catalyst in Acid. *J. Am. Chem. Soc.* **2014**, *136* (16), 6002−6010.

(7) Luo, W.; Hu, J.; Diao, H.; Schwarz, B.; Streb, C.; Song, Y.-F. Stabile Polyoxometallat-Nickelschaum-Elektroden Für Elektrochemische Sauerstoffentwicklung Im Alkalischen Milieu. *Angew. Chem.* **2017**, *129* (18), 5023−5026.

(8) Zhang, R.; Pan, L.; Guo, B.; Huang, Z. F.; Chen, Z.; Wang, L.; Zhang, X.; Guo, Z.; Xu, W.; Loh, K. P.; Zou, J. J. Tracking the Role of Defect Types in Co3O4 Structural Evolution and Active Motifs during Oxygen Evolution Reaction. *J. Am. Chem. Soc.* **2023**, *145*, 2271−2281.

(9) Ling, T.; Zhang, T.; Ge, B.; Han, L.; Zheng, L.; Lin, F.; Xu, Z.; Hu, W. B.; Du, X. W.; Davey, K.; Qiao, S. Z. Well-Dispersed Nickel- and Zinc-Tailored Electronic Structure of a Transition Metal Oxide for Highly Active Alkaline Hydrogen Evolution Reaction. *Adv. Mater.* **2019**, *31* (16), No. 1807771, DOI: 10.1002/adma.201807771.

(10) Gong, R.; Gao, D.; Liu, R.; Sorsche, D.; Biskupek, J.; Kaiser, U.; Rau, S.; Streb, C. Self-Activation of a Polyoxometalate-Derived Composite Electrocatalyst for the Oxygen Evolution Reaction. *ACS Appl. Energy Mater.* **2021**, *4* (11), 12671−12676.

(11) Li, N.; Bediako, D. K.; Hadt, R. G.; Hayes, D.; Kempa, T. J.; Von Cube, F.; Bell, D. C.; Chen, L. X.; Nocera, D. G. Influence of Iron Doping on Tetravalent Nickel Content in Catalytic Oxygen Evolving Films. *Proc. Natl. Acad. Sci. U.S.A.* **2017**, *114* (7), 1486−1491.

(12) She, Z. W.; Kibsgaard, J.; Dickens, C. F.; Chorkendorff, I.; Nørskov, J. K.; Jaramillo, T. F. Combining Theory and Experiment in Electrocatalysis: Insights into Materials Design. *Science* **2017**, *355*, No. eaad4998, DOI: 10.1126/science.aad4998.

(13) Song, F.; Bai, L.; Moysiadou, A.; Lee, S.; Hu, C.; Liardet, L.; Hu, X. Transition Metal Oxides as Electrocatalysts for the Oxygen Evolution Reaction in Alkaline Solutions: An Application-Inspired Renaissance. *J. Am. Chem. Soc.* **2018**, *140* (25), 7748−7759.

(14) Grimaud, A.; Hong, W. T.; Shao-Horn, Y.; Tarascon, J. M. Anionic Redox Processes for Electrochemical Devices. *Nat. Mater.* **2016**, *15*, 121−126, DOI: 10.1038/nmat4551.

(15) Dau, H.; Limberg, C.; Reier, T.; Risch, M.; Roggan, S.; Strasser, P. The Mechanism of Water Oxidation: From Electrolysis via Homogeneous to Biological Catalysis. *ChemCatChem* **2010**, *2*, 724−761.

(16) Doyle, R. L.; Lyons, M. E. G. Kinetics and Mechanistic Aspects of the Oxygen Evolution Reaction at Hydrous Iron Oxide Films in Base. *J. Electrochem. Soc.* **2013**, *160* (2), H142−H154.

(17) Jiao, Y.; Zheng, Y.; Jaroniec, M.; Qiao, S. Z. Design of Electrocatalysts for Oxygen- and Hydrogen-Involving Energy Conversion Reactions. *Chem. Soc. Rev.* **2015**, *44*, 2060−2086, DOI: 10.1039/c4cs00470a.

(18) Benck, J. D.; Hellstern, T. R.; Kibsgaard, J.; Chakthranont, P.; Jaramillo, T. F. Catalyzing the Hydrogen Evolution Reaction (HER) with Molybdenum Sulfide Nanomaterials. *ACS Catal.* **2014**, *4*, 3957−3971, DOI: 10.1021/cs500923c.

(19) Liu, X.; Meng, J.; Zhu, J.; Huang, M.; Wen, B.; Guo, R.; Mai, L. Comprehensive Understandings into Complete Reconstruction of Precatalysts: Synthesis, Applications, and Characterizations. *Adv. Mater.* **2021**, *33* (32), No. 2007344, DOI: 10.1002/adma.202007344.

(20) Zhao, Y.; Saseendran, D. P. A.; Huang, C.; Triana, C. A.; Marks, W. R.; Chen, H.; Zhao, H.; Patzke, G. R. Oxygen Evolution/ Reduction Reaction Catalysts: From *In Situ* Monitoring and Reaction Mechanisms to Rational Design. *Chem. Rev.* **2023**, *123* (9), 6257−6358.

(21) Ahn, H. S.; Bard, A. J. Surface Interrogation Scanning Electrochemical Microscopy of Ni$_{1−x}$Fe$_x$OOH (0 < x < 0.27) Oxygen Evolving Catalyst: Kinetics of the "Fast" Iron Sites. *J. Am. Chem. Soc.* **2016**, *138* (1), 313−318.

(22) Peña, N. O.; Ihiawakrim, D.; Han, M.; Lassalle-Kaiser, B.; Carenco, S.; Sanchez, C.; Laberty-Robert, C.; Portehault, D.; Ersen, O. Morphological and Structural Evolution of Co$_3$O$_4$ Nanoparticles Revealed by *in Situ* Electrochemical Transmission Electron Microscopy during Electrocatalytic Water Oxidation. *ACS Nano* **2019**, *13* (10), 11372−11381.

(23) Handoko, A. D.; Wei, F.; Jenndy; Yeo, B. S.; Seh, Z. W. Understanding Heterogeneous Electrocatalytic Carbon Dioxide Reduction through Operando Techniques. *Nat. Catal.* **2018**, *1*, 922−934, DOI: 10.1038/s41929-018-0182-6.

(24) Tung, C.-W.; Hsu, Y.-Y.; Shen, Y.-P.; Zheng, Y.; Chan, T.-S.; Sheu, H.-S.; Cheng, Y.-C.; Chen, H. M. Reversible Adapting Layer Produces Robust Single-Crystal Electrocatalyst for Oxygen Evolution. *Nat. Commun.* **2015**, *6* (1), No. 8106.

(25) Stoerzinger, K. A.; Hong, W. T.; Crumlin, E. J.; Bluhm, H.; Shao-Horn, Y. Insights into Electrochemical Reactions from Ambient Pressure Photoelectron Spectroscopy. *Acc. Chem. Res.* **2015**, *48* (11), 2976−2983.

(26) Chen, J. Y. C.; Dang, L.; Liang, H.; Bi, W.; Gerken, J. B.; Jin, S.; Alp, E. E.; Stahl, S. S. Operando Analysis of NiFe and Fe Oxyhydroxide Electrocatalysts for Water Oxidation: Detection of Fe^{4+} by Mössbauer Spectroscopy. *J. Am. Chem. Soc.* **2015**, *137* (48), 15090−15093.

(27) Reuss, T.; Lalithambika, S. S. N.; David, C.; Döring, F.; Jooss, C.; Risch, M.; Techert, S. Advancements in Liquid Jet Technology and X-Ray Spectroscopy for Understanding Energy Conversion Materials during Operation. *Acc. Chem. Res.* **2023**, *56* (3), 203−214.

(28) Shackleford, S. G. D.; Boxall, C.; Port, S. N.; Taylor, R. J. An in Situ Electrochemical Quartz Crystal Microbalance Study of Polycrystalline Gold Electrodes in Nitric Acid Solution. *J. Electroanal. Chem.* **2002**, *538−539*, 109−119.

(29) Timoshenko, J.; Cuenya, B. R. *In Situ/Operando* Electrocatalyst Characterization by X-Ray Absorption Spectroscopy. *Chem. Rev.* **2021**, *121* (2), 882−961.

(30) Yang, Y.; Wang, Y.; Xiong, Y.; Huang, X.; Shen, L.; Huang, R.; Wang, H.; Pastore, J. P.; Yu, S.-H.; Xiao, L.; Brock, J. D.; Zhuang, L.; Abruña, H. D. In Situ X-Ray Absorption Spectroscopy of a Synergistic Co−Mn Oxide Catalyst for the Oxygen Reduction Reaction. *J. Am. Chem. Soc.* **2019**, *141* (4), 1463−1466.

(31) Maurizio, C.; El Habra, N.; Rossetto, G.; Merlini, M.; Cattaruzza, E.; Pandolfo, L.; Casarin, M. XAS and GIXRD Study of Co Sites in CoAl2O4 Layers Grown by MOCVD. *Chem. Mater.* **2010**, *22* (5), 1933−1942.

(32) Gao, D.; Liu, R.; Biskupek, J.; Kaiser, U.; Song, Y.; Streb, C. Modular Design of Noble-Metal-Free Mixed Metal Oxide Electrocatalysts for Complete Water Splitting. *Angew. Chem.* **2019**, *131* (14), 4692−4696.

(33) Neel, J. V.; Schull, W. J.; McDonald, D. J.; Morton, N. E.; Kodani, M.; Takeshima, K.; Anderson, R. C.; Wood, J.; Brewer, R.; Wright, S.; Yamazaki, J.; Suzuki, M.; Kitamura, S. The Effect of Exposure to the Atomic Bombs on Pregnancy Termination in Hiroshima and Nagasaki: Preliminary Report. *Science* **1953**, *118* (3071), 537−541.

(34) Lv, H.; Song, J.; Geletii, Y. V.; Vickers, J. W.; Sumliner, J. M.; Musaev, D. G.; Kögerler, P.; Zhuk, P. F.; Bacsa, J.; Zhu, G.; Hill, C. L. An Exceptionally Fast Homogeneous Carbon-Free Cobalt-Based Water Oxidation Catalyst. *J. Am. Chem. Soc.* **2014**, *136* (26), 9268−9271.

(35) Villars, P.; Cenzual, K.; Daams, J.; Gladyshevskii, R.; Shcherban, O.; Dubenskyy, V.; Kuprysyuk, V.; Savysyuk, I. K5-[CoW12O40]•20H2O. In *Structure Types. Part 9: Space Groups (148) R-3 - (141) I41/amd*; Springer, 2010; pp 515−516.

(36) Hilbrig, F.; Gobel, H. E.; Knó, H.; Schmelz, H.; Lengeler, B. Power Generation Group KWU, Siemens AG, Otto Hahn Ring 6, 8000 München 83, 1991. https://pubs.acs.org/sharingguidelines.

(37) Yamazoe, S.; Hitomi, Y.; Shishido, T.; Tanaka, T. XAFS Study of Tungsten L1- And L3-Edges: Structural Analysis of WO3 Species Loaded on TiO2 as a Catalyst for Photo-Oxidation of NH3. *J. Phys. Chem. C* **2008**, *112* (17), 6869−6879.

(38) Weng, Z.; Wu, Y.; Wang, M.; Jiang, J.; Yang, K.; Huo, S.; Wang, X.-F.; Ma, Q.; Brudvig, G. W.; Batista, V. S.; Liang, Y.; Feng, Z.; Wang, H. Active Sites of Copper-Complex Catalytic Materials for Electrochemical Carbon Dioxide Reduction. *Nat. Commun.* **2018**, *9* (1), No. 415.

(39) Khemthong, P.; Photai, P.; Grisdanurak, N. Structural Properties of CuO/TiO2 Nanorod in Relation to Their Catalytic Activity for Simultaneous Hydrogen Production under Solar Light. *Int. J. Hydrogen Energy* **2013**, *38* (36), 15992−16001.

(40) Gaur, A.; Shrivastava, B. D.; Joshi, S. K. Copper K-Edge XANES of Cu(I) and Cu(II) Oxide Mixtures. *J. Phys.: Conf Ser.* **2009**, *190*, No. 012084.

(41) Ravel, B.; Newville, M. *ATHENA, ARTEMIS, HEPHAESTUS*: Data Analysis for X-Ray Absorption Spectroscopy Using *IFEFFIT*. *J. Synchrotron Radiat.* **2005**, *12* (4), 537−541.

(42) Wang, M.; Feng, Z. Pitfalls in X-Ray Absorption Spectroscopy Analysis and Interpretation: A Practical Guide for General Users. *Curr. Opin. Electrochem.* **2021**, *30*, No. 100803.

(43) Sharma, A.; Varshney, M.; Park, J.; Ha, T.-K.; Chae, K.-H.; Shin, H.-J. XANES, EXAFS and Photocatalytic Investigations on Copper Oxide Nanoparticles and Nanocomposites. *RSC Adv.* **2015**, *5* (28), 21762−21771.

(44) Hsiao, M. C.; Wang, H. P.; Yang, Y. W. EXAFS and XANES Studies of Copper in a Solidified Fly Ash. *Environ. Sci. Technol.* **2001**, *35* (12), 2532−2535.

(45) Abeysinghe, D.; Smith, M. D.; Yeon, J.; Tran, T. T.; Sena, R. P.; Hadermann, J.; Halasyamani, P. S.; zur Loye, H.-C. Crystal Growth and Structure Analysis of Ce$_{18}$W$_{10}$O$_{57}$: A Complex Oxide Containing Tungsten in an Unusual Trigonal Prismatic Coordination Environment. *Inorg. Chem.* **2017**, *56* (5), 2566−2575.

(46) Jerkiewicz, G. Applicability of Platinum as a Counter-Electrode Material in Electrocatalysis Research. *ACS Catal.* **2022**, *12* (4), 2661−2670.

(47) Dau, H.; Liebisch, P.; Haumann, M. X-Ray Absorption Spectroscopy to Analyze Nuclear Geometry and Electronic Structure of Biological Metal Centers-Potential and Questions Examined with Special Focus on the Tetra-Nuclear Manganese Complex of Oxygenic Photosynthesis. *Anal. Bioanal. Chem.* **2003**, *376* (5), 562−583.

(48) Sprague-Klein, E. A.; He, X.; Mara, M. W.; Reinhart, B. J.; Lee, S.; Utschig, L. M.; Mulfort, K. L.; Chen, L. X.; Tiede, D. M. Photo-Electrochemical Effect in the Amorphous Cobalt Oxide Water Oxidation Catalyst Cobalt−Phosphate (CoPi). *ACS Energy Lett.* **2022**, *7* (9), 3129−3138.

(49) Hunault, M.; Vercamer, V.; Haverkort, M. W.; Arrio, M.-A.; Brouder, C.; Calas, G.; Juhin, A. Tracking the Signature of Low Symmetry Environments in the XAS *K* Pre-Edge. *J. Phys.: Conf. Ser.* **2016**, *712*, No. 012005.

(50) Haase, F. T.; Bergmann, A.; Jones, T. E.; Timoshenko, J.; Herzog, A.; Jeon, H. S.; Rettenmaier, C.; Cuenya, B. R. Size Effects and Active State Formation of Cobalt Oxide Nanoparticles during the Oxygen Evolution Reaction. *Nat. Energy* **2022**, *7* (8), 765−773.

(51) Esmaeilirad, M.; Kondori, A.; Song, B.; Belmonte, A. R.; Wei, J.; Kucuk, K.; Khanvilkar, S. M.; Efimoff, E.; Chen, W.; Segre, C. U.; Shahbazian-Yassar, R.; Asadi, M. Oxygen Functionalized Copper Nanoparticles for Solar-Driven Conversion of Carbon Dioxide to Methane. *ACS Nano* **2020**, *14* (2), 2099−2108.

(52) Frenkel, A. I.; Hills, C. W.; Nuzzo, R. G. A View from the Inside: Complexity in the Atomic Scale Ordering of Supported Metal Nanoparticles. *J. Phys. Chem. B* **2001**, *105* (51), 12689−12703.

(53) Frenkel, A. Solving the 3D Structure of Metal Nanoparticles. *Z. Kristallogr. - Cryst. Mater.* **2007**, *222* (11), 605−611.

(54) Clausena, B. S.; Topsøe, H.; Hansen, L. B.; Stoltze, P.; Nørskov, J. K. Determination of Metal Particle Sizes from EXAFS. *Catal. Today* **1994**, *21* (1), 49−55.

(55) Durst, J.; Siebel, A.; Simon, C.; Hasché, F.; Herranz, J.; Gasteiger, H. A. New Insights into the Electrochemical Hydrogen Oxidation and Evolution Reaction Mechanism. *Energy Environ. Sci.* **2014**, *7* (7), 2255−2260.

(56) Sheng, W.; Zhuang, Z.; Gao, M.; Zheng, J.; Chen, J. G.; Yan, Y. Correlating Hydrogen Oxidation and Evolution Activity on Platinum at Different PH with Measured Hydrogen Binding Energy. *Nat. Commun.* **2015**, *6* (1), No. 5848.

(57) Anantharaj, S.; Noda, S.; Jothi, V. R.; Yi, S.; Driess, M.; Menezes, P. W. Strategies and Perspectives to Catch the Missing Pieces in Energy-Efficient Hydrogen Evolution Reaction in Alkaline Media. *Angew. Chem., Int. Ed.* **2021**, *60* (35), 18981−19006.

(58) Lassalle-Kaiser, B.; Zitolo, A.; Fonda, E.; Robert, M.; Anxolabéhère-Mallart, E. In Situ Observation of the Formation and Structure of Hydrogen-Evolving Amorphous Cobalt Electrocatalysts. *ACS Energy Lett.* **2017**, *2* (11), 2545−2551.

(59) Huang, C.; Sasaki, K.; Raja, D. S.; Hsieh, C.; Wu, Y.; Su, J.; Cheng, C.; Cheng, P.; Lin, S.; Choi, Y.; Lu, S. Twinning Enhances Efficiencies of Metallic Catalysts toward Electrolytic Water Splitting. *Adv. Energy Mater.* **2021**, *11* (46), No. 2101827, DOI: 10.1002/aenm.202101827.

(60) Ye, L.; Wen, Z. Self-Supported Three-Dimensional Cu/Cu$_2$O−CuO/RGO Nanowire Array Electrodes for an Efficient Hydrogen Evolution Reaction. *Chem. Commun.* **2018**, *54* (49), 6388−6391.

(61) Putra, R. P.; Horino, H.; Rzeznicka, I. I. An Efficient Electrocatalyst for Oxygen Evolution Reaction in Alkaline Solutions

Derived from a Copper Chelate Polymer via In Situ Electrochemical Transformation. *Catalysts* **2020**, *10* (2), No. 233.

(62) Kumar, B.; Saha, S.; Ojha, K.; Ganguli, A. K. A Facile One Step Synthesis of Cu/Cu2O Nanocomposites: Enhanced Hydrogen/ Oxygen Evolution. *Mater. Res. Bull.* **2015**, *64*, 283−287.

(63) Shinagawa, T.; Garcia-Esparza, A. T.; Takanabe, K. Insight on Tafel Slopes from a Microkinetic Analysis of Aqueous Electrocatalysis for Energy Conversion. *Sci. Rep.* **2015**, *5* (1), No. 13801.

(64) Yang, H.; Gao, S.; Rao, D.; Zhang, C.; Zhou, X.; Yang, S.; Ye, J.; Yang, S.; Lai, F.; Yan, X. Non-Metallic Electronic Regulation in CuCo Oxy-/Thio-Spinel as Advanced Oxygen Evolution Electrocatalysts. *Sci. China: Chem.* **2021**, *64* (1), 101−108.

(65) Chauhan, M.; Reddy, K. P.; Gopinath, C. S.; Deka, S. Copper Cobalt Sulfide Nanosheets Realizing a Promising Electrocatalytic Oxygen Evolution Reaction. *ACS Catal.* **2017**, *7* (9), 5871−5879.

(66) Chen, T.; Ren, H.; Li, L.; Tan, W.; He, H. Synergistic Cobalt− Copper Metal−Organic Framework-Derived Oxide Electrocatalyst for Efficient Oxygen Evolution Reaction. *Mater. Chem. Phys.* **2024**, *313*, No. 128689.